Supporting Information

Oxygen Insertion at Cage Center: An Unconventional Tuning Strategy for Enhancing the Photocatalytic Performance of Atomically Precise Copper Cluster Cocatalysts

Yun-Dong Cao,[a] Di Yin,[a] Ming-Liang Wang,[a] Hong Liu,*[a] Yi Feng,[a] Lin-Lin Fan,*[a] Cai-Li Lv [a] and Guang-Gang Gao *[a]

[a] *School of Materials Science and Engineering, University of Jinan, 250022, Jinan, China*

* Corresponding authors

E-mail: mse_liuh@ujn.edu.cn; mse_fanll@ujn.edu.cn; mse_gaogg@ujn.edu.cn.

Table of Contents

Fig. S18. The FTIR spectrum of **[Cu_{14}][O@Cu_{14}]@g-C_3N_4(OH)** after photocatalytic H_2 evolution.

Fig. S19. XPS spectra for Cu 2p (a), S 2p (b), P 2p (c) and O 1s (d) of **[Cu_{14}][O@Cu_{14}]@g-C_3N_4(OH)** after photocatalytic H_2 evolution.

Fig. S20. DPV of **Cu_{14}** (a), **O@Cu_{14}** (b) and **[Cu_{14}][O@Cu_{14}]** (c). The UPS spectra of **Cu_{14}** (d), **O@Cu_{14}** (e) and **[Cu_{14}][O@Cu_{14}]** (f). The energies of the secondary electron cutoff edge of **Cu_{14}** (g), **O@Cu_{14}** (h) and **[Cu_{14}][O@Cu_{14}]** (i). The energies of the injection potential barrier edge of **Cu_{14}** (j), **O@Cu_{14}** (k) and **[Cu_{14}][O@Cu_{14}]** (l).

Fig. S21. (a) The UV-Vis diffuse reflectance spectrum of g-C_3N_4(OH). (b) The bond gap of g-C_3N_4(OH) estimated by the Tauc plot of KubelkaMunk function: $((\alpha h\nu)^2 = C(h\nu - E_g))$. (c) The UPS spectra g-$C_3N_4$(OH). (d) The energies of the secondary electron cutoff edge of g-C_3N_4(OH). (e) and the energies of the injection potential barrier edge of g-C_3N_4(OH).

Supporting tables

Table S1. Metric Data of the Known Clusters of with Cu_8 cages encapsulating central atoms.

Table S2. Comparison of photocatalytic H_2 evolution activities of crystalline Cu-based photocatalysts.

Experimental methods

Chemicals. All chemicals are commercially available without further purification. Benzyl mercaptan, Tetrakis(acetonitrile)copper(I) hexafluorophosphate, acetonitrile (HPLC grade) and melamine were obtained from Sigma Aldrich. $LiNO_3$ and borane-tert-butylamine complex were obtained from aladdin. Tris(4-fluorophenyl)phosphine, sodium hydroxide, dichloromethane (CH_2Cl_2, HPLC grade), triethanolamine and methanol (HPLC grade) were obtained from Macklin.

Single crystal X-ray diffraction analysis. Single-Crystal X-ray Diffraction Analysis measurements were performed on a Rigaku XtaLAB Pro diffractometer with Mo-Kα radiation (λ = 0.71073 Å) and Cu-Kα radiation (λ = 1.54186 Å) at 173 K. Data collection and reduction were performed using the program CrysAlisPro[1]. The intensities were corrected for absorption using the empirical method implemented in SCALE3 ABSPACK scaling algorithm. The structures were solved with intrinsic phasing methods (SHELXT-2015)[2], and refined by full-matrix least-squares on F^2 using OLEX2,[3] which utilizes the SHELXL-2015 module.[3] The crystal structures are visualized by DIAMOND 3.2.[4]

Materials and characterization. A Nicolet 6700 spectrophotometer was used to record the FTIR spectra with KBr as the phragmoid auxiliary material. The phases of the samples were tested by Rigaku SmartLab 9KW X-ray diffraction (XRD). High resolution transmission electron microscopy (HRTEM) diagrams patterns were recorded on a JEM-2100Plus transmission electron microscope instrument with 200 kV of accelerating voltage. A CEL-SPH2N photo catalysis system was used to obtain performance of water splitting reaction. A CHI660E electrochemical workbench was carried out to collect electrochemical performances. UV-Vis diffuse reflectance spectra were measured using a Shimazu UV-visible spectrophotometer UV-8000. The Fl emission spectra was detected by a shimadzu fluorescence spectrophotometer RF-6000 with the excitation wavelength at 320 nm. XPS and UPS data were obtained using a Thermo Fisher ESCALAB Xi+ spectrometer.

Photocatalysis. A CEL-SPH2N photo catalysis system was used to collect the performances of photocatalytic activities. Argon was purged through the reactor for 1 h before reaction to remove the residual air. During the photocatalytic experiment, A 300 W Xe lamp (CELHXF300) with a 400 nm filter was used as the light source (λ>400 nm) to trigger the photocatalytic generation of H_2 with the efficient irradiation area of 15.90 cm^2. Typically, in the photocatalytic H_2 evolution reaction, 10 mg of as-prepared photocatalysts were added to the mixed solution (water: TEOA = 4: 1) with continuous stirring. The solution volume was kept at 50 mL. During the whole experiment, the reactor was treated with a cooling pump to maintain the temperature at 6 °C. The amount of generated gas was detected by the GC7920-TF2ZA2 gas chromatograph (TCD, N2 gas carrier). Blank experiments revealed no appreciable gas evolution without irradiation or photocatalysts.

Apparent Quantum Yield (AQY) tests. The AQY for photocatalytic H_2 evolution were collected under the illumination of a 300 W Xe lamp (CELHXF300) with bandpass filters (λ = 400±10, 420±10, 450±10, 550±10, 650±10 nm) used to provide the monochromatic light. A CEL-NP2000 irradiation meter was use to collect light intensity and incident photons. Generally, for a photocatalytic H_2 evolution system, the AQY value was calculated according to the following equation:

$$AQY(\%) = \frac{Number\ of\ reacted\ electrons}{Number\ of\ incident\ photons} \times 100\%$$
$$= \frac{Number\ of\ evolved\ hydrogen\ molecules \times 2}{Number\ of\ incident\ photons}$$

Transient photocurrent response tests. The transient photocurrent response curves of photocatalysts were measured by a CHI660E electrochemical workstation under the same light with a photocatalytic test in 0.1 M Na_2SO_4 in a three-electrode cell, in which the Ag/AgCl electrode and Pt wire were used as reference and counter electrodes, respectively. The preparation of the working electrode was as follows: 5 mg of catalyst was added into the system of water (650 μL), Nafion (50 μL) and Isopropyl alcohol (350 μL) before ultrasonic dispersion for 30 min. Afterwards, the resultant mixture (5 μL) was dried on the surface of glassy carbon.

UV-Vis diffuse reflectance spectrum tests. UV-Vis diffuse reflectance spectra were measured using a Shimazu UV-visible spectrophotometer UV-8000. The solid samples were ground and crushed before testing. Background calibration and baseline calibration were performed on the instrument before sample testing. The band gaps were extracted by Kubelka-Munk method.

Supporting figures

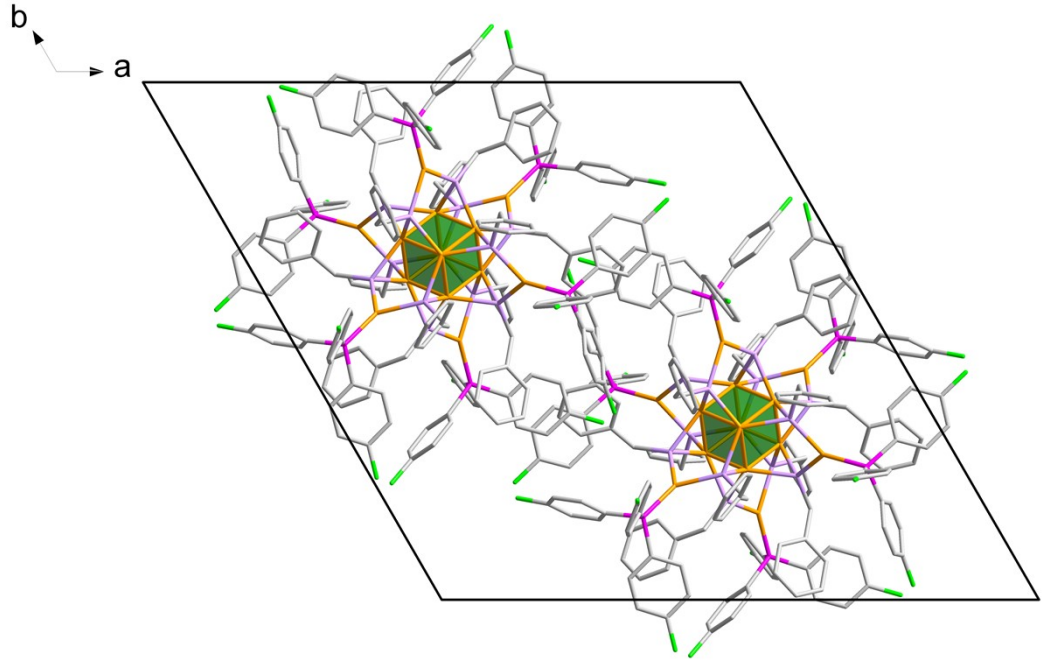

Fig. S1. Packing mode of **Cu_{14}**. Color code: Cu, orange; C, gray; S, purple; P, pink; O, red; F, green.

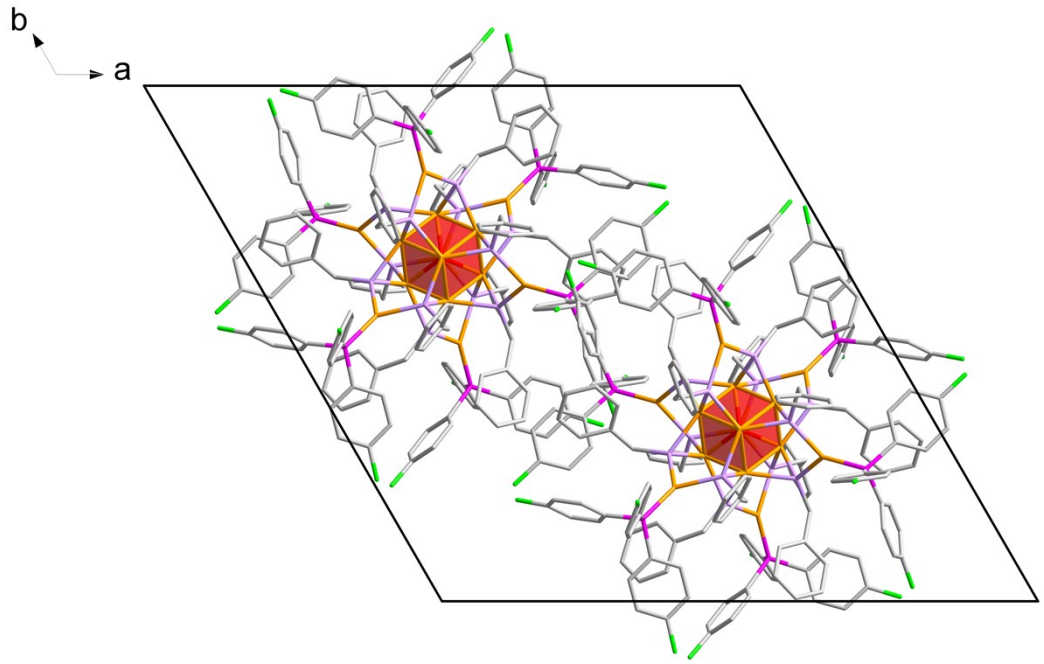

Fig. S2. Packing mode of **O@Cu$_{14}$**. Color code: Cu, orange; C, gray; S, purple; P, pink; O, red; F, green.

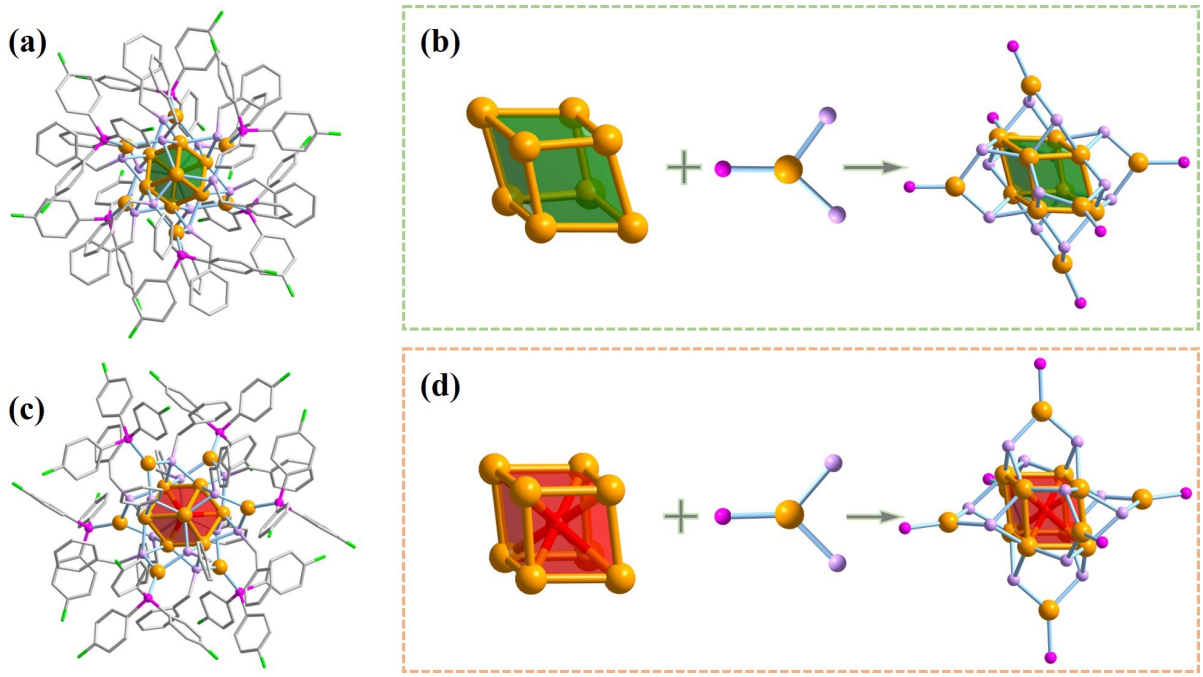

Fig. S3. Total crystal structures of **[Cu_{14}]** (a) and **[O@Cu_{14}]** (c). Cluster core structures of **[Cu_{14}]** (b) and **[O@Cu_{14}]** (d). Color code: Cu, orange; C, gray; S, purple; P, pink; O, red; F, green.

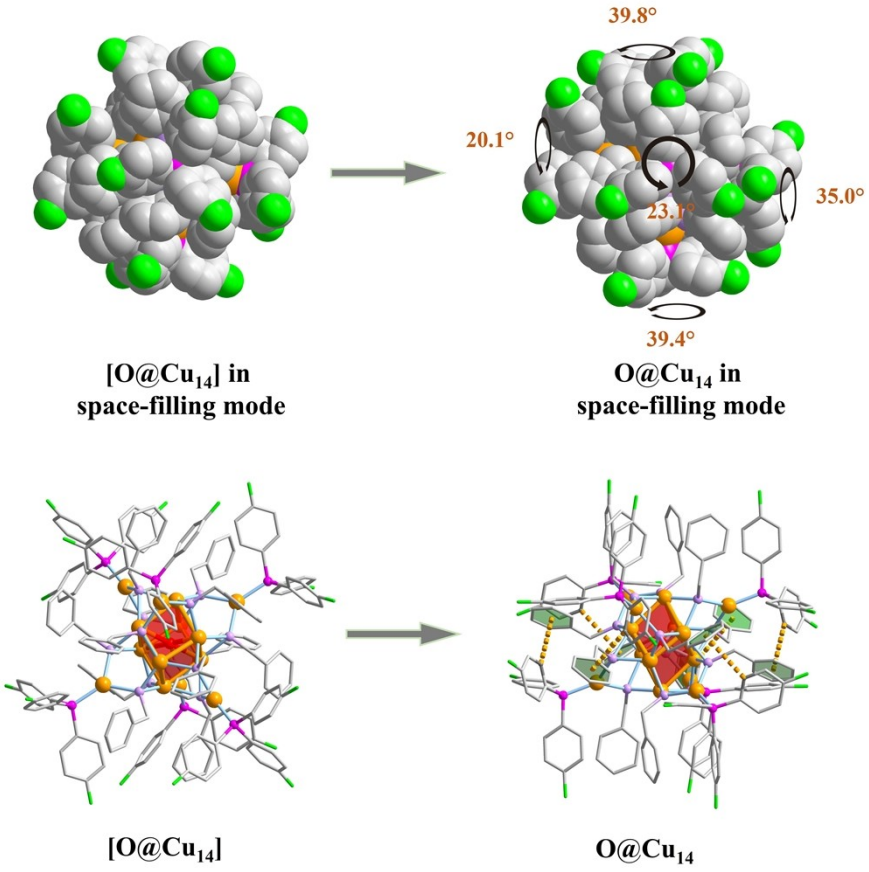

Fig. S4. Presentation of the structures of **[O@Cu$_{14}$]** and **O@Cu$_{14}$** in space-filling mode and the π-π interactions. Color code: Cu, orange; C, gray; S, purple; P, pink; O, red; F, green.

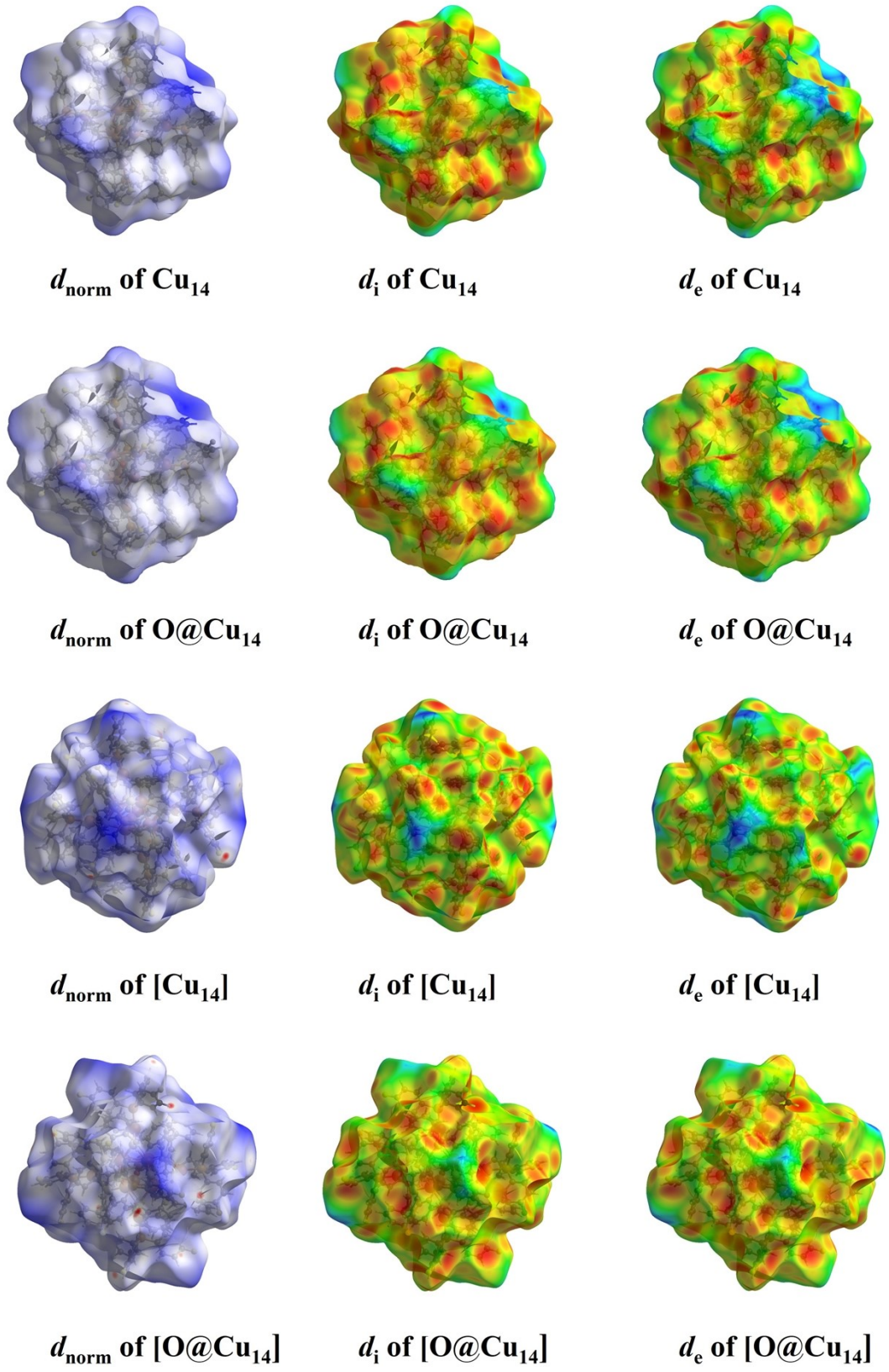

Fig. S5. Hirshfeld surfaces mapped over d_{norm}, d_e and d_i for **Cu_{14}**, **$O@Cu_{14}$**, **$[Cu_{14}]$** and **$[O@Cu_{14}]$**.

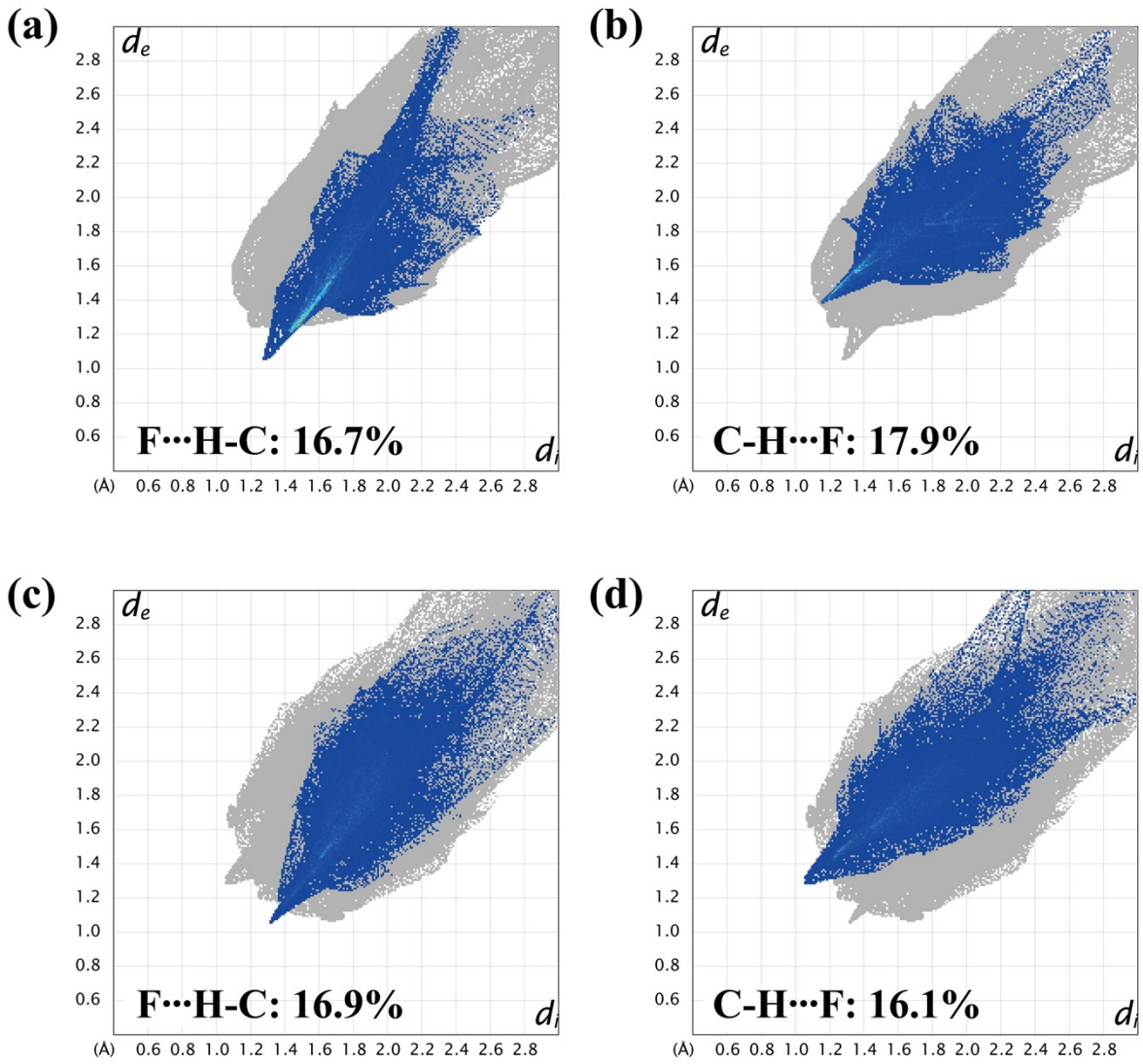

Fig. S6. Fingerprint plots corresponding to C-H···F contacts involved in the structure of **[Cu_{14}]** and **[O@Cu_{14}]**.

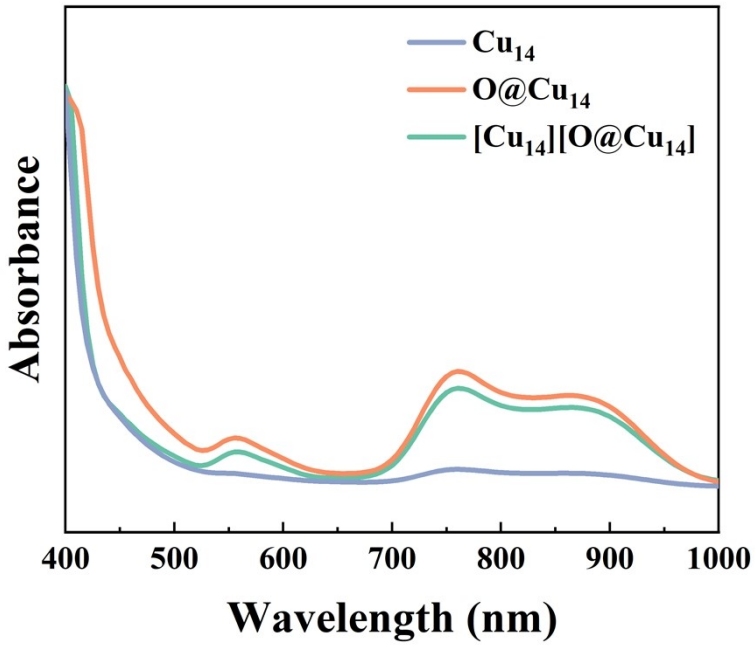

Fig. S7. UV-Vis absorption spectra of **Cu_{14}**, **$O@Cu_{14}$** and **$[Cu_{14}][O@Cu_{14}]$**.

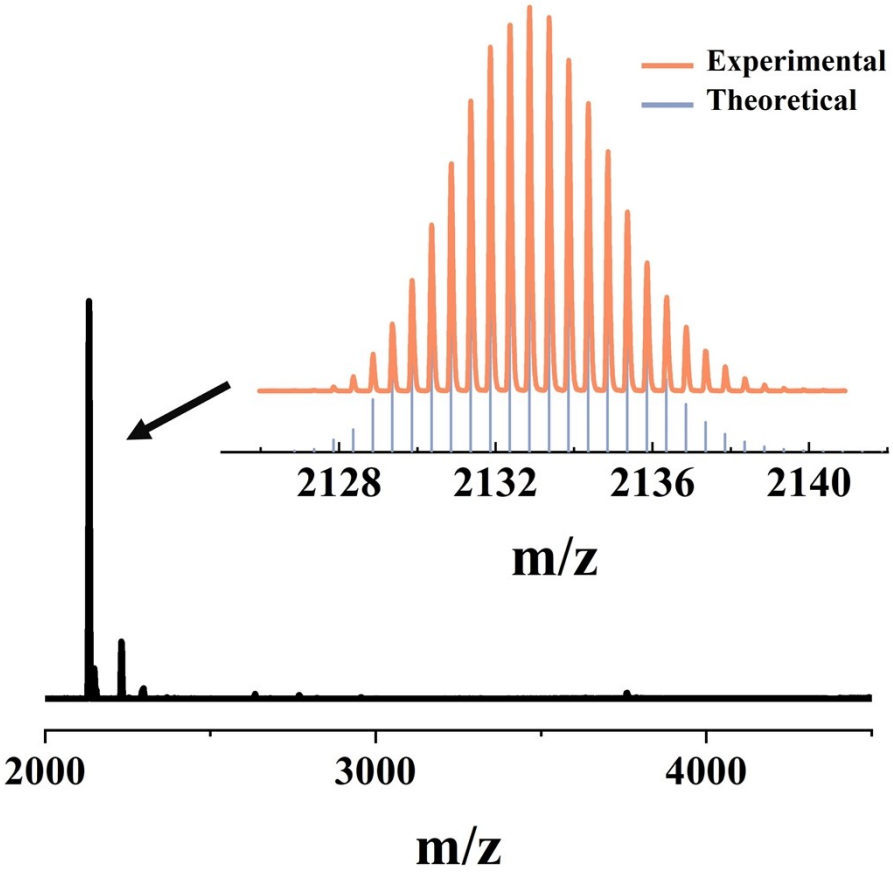

Fig. S8. The cation-mode electrospray mass spectrometry spectra of $\mathbf{Cu_{14}}$.

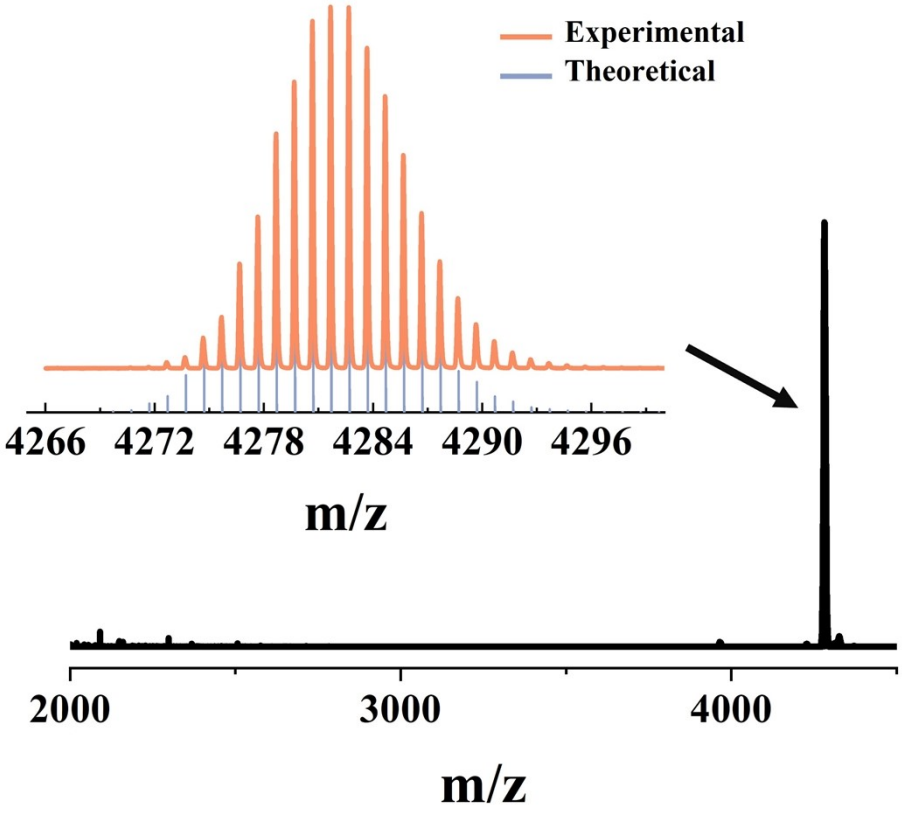

Fig. S9. The cation-mode electrospray mass spectrometry spectra of **O@Cu$_{14}$**.

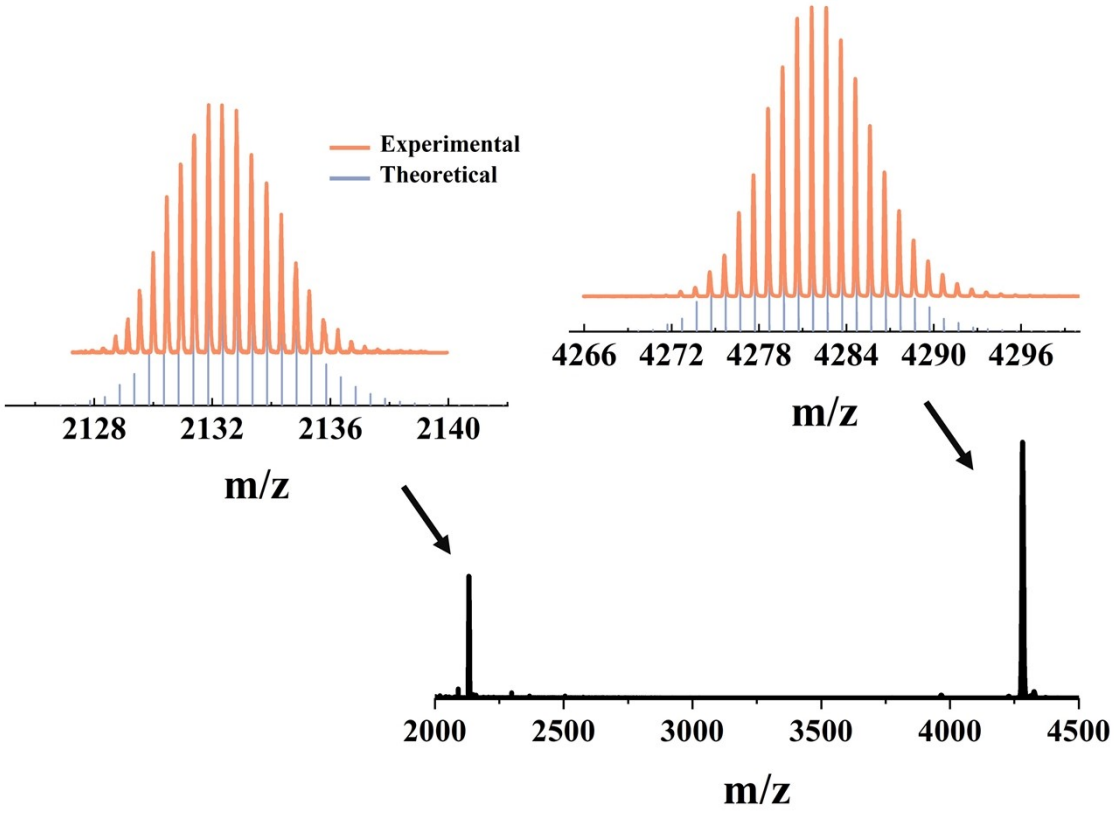

Fig. S10. The cation-mode electrospray mass spectrometry spectra of **[Cu_{14}][O@Cu_{14}]**.

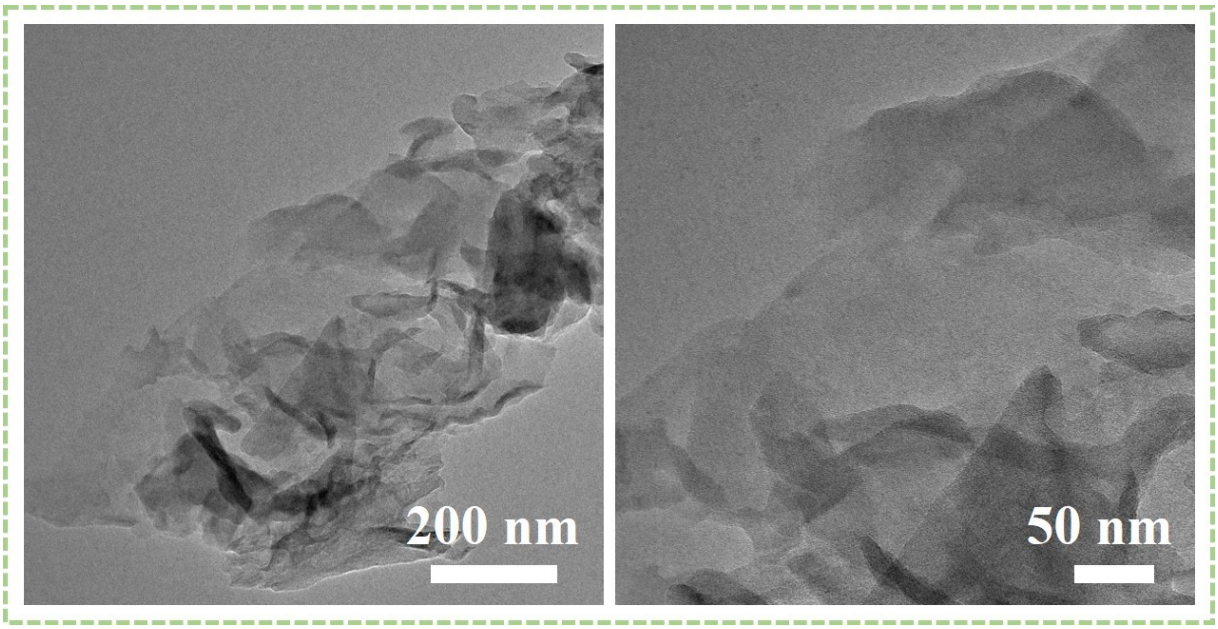

Fig. S11. HRTEM images of g-C_3N_4(OH) nanosheets.

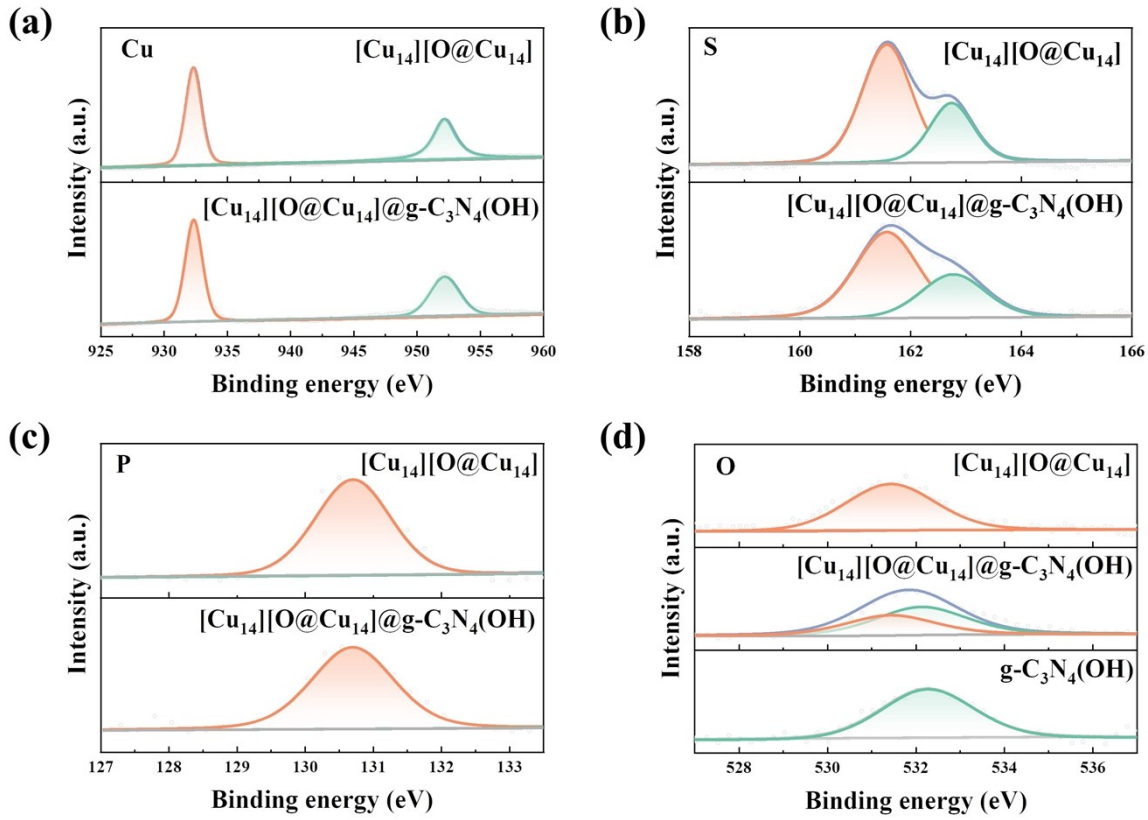

Fig. S12. XPS spectra for Cu 2p (a), S 2p (b) and P 2p (c) of **[Cu_{14}][O@Cu_{14}]** and **[Cu_{14}][O@Cu_{14}]@g-C_3N_4(OH)**. (d) XPS spectra for O 1s of **[Cu_{14}][O@Cu_{14}]**, **[Cu_{14}][O@Cu_{14}]@g-C_3N_4(OH)** and g-C_3N_4(OH). XPS spectra of O 1s were collected after Ar^+ sputtering.

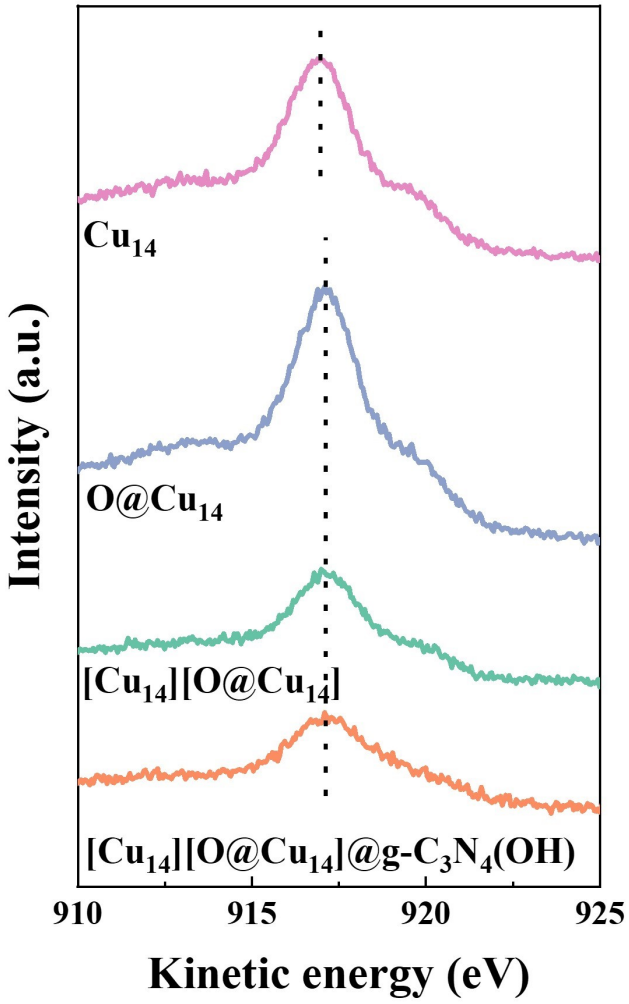

Fig. S13. The Auger Cu LMM spectra of **Cu_{14}**, **$O@Cu_{14}$**, **$[Cu_{14}][O@Cu_{14}]$** and **$[Cu_{14}][O@Cu_{14}]@g\text{-}C_3N_4(OH)$**.

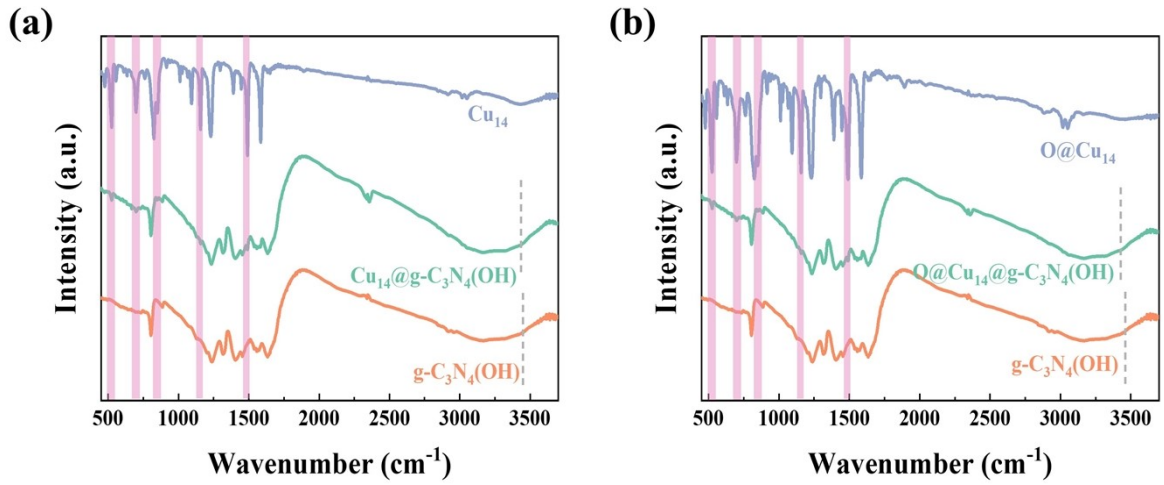

Fig. S14. (a) The FTIR spectra of **Cu_{14}**, **Cu_{14}@g-C_3N_4(OH)** and g-C_3N_4(OH) nanosheets. (b) The FTIR spectra of **O@Cu_{14}**, **O@Cu_{14}@g-C_3N_4(OH)** and g-C_3N_4(OH) nanosheets.

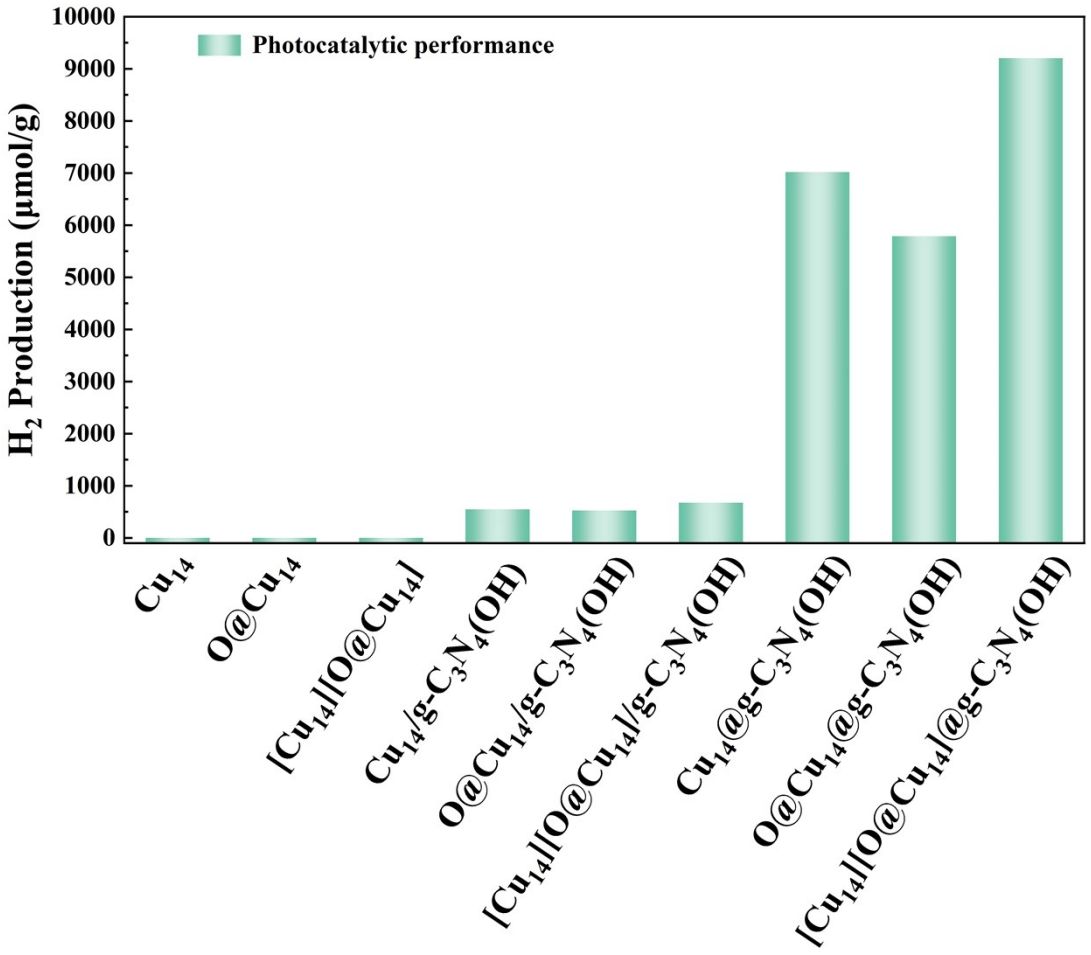

Fig. S15. Photocatalytic performance of copper clusters (**Cu_{14}**, **$O@Cu_{14}$** and **$[Cu_{14}][O@Cu_{14}]$**), physically mixed copper clusters and g-C_3N_4 nanosheets (**Cu_{14}**/g-C_3N_4(OH), **$O@Cu_{14}$**/g-C_3N_4(OH) and **$[Cu_{14}][O@Cu_{14}]$**/g-C_3N_4(OH)), the as-prepared photocatalysts (**Cu_{14}@g-C_3N_4(OH)**, **$O@Cu_{14}$@g-C_3N_4(OH)**, **$[Cu_{14}][O@Cu_{14}]$@g-C_3N_4(OH)**).

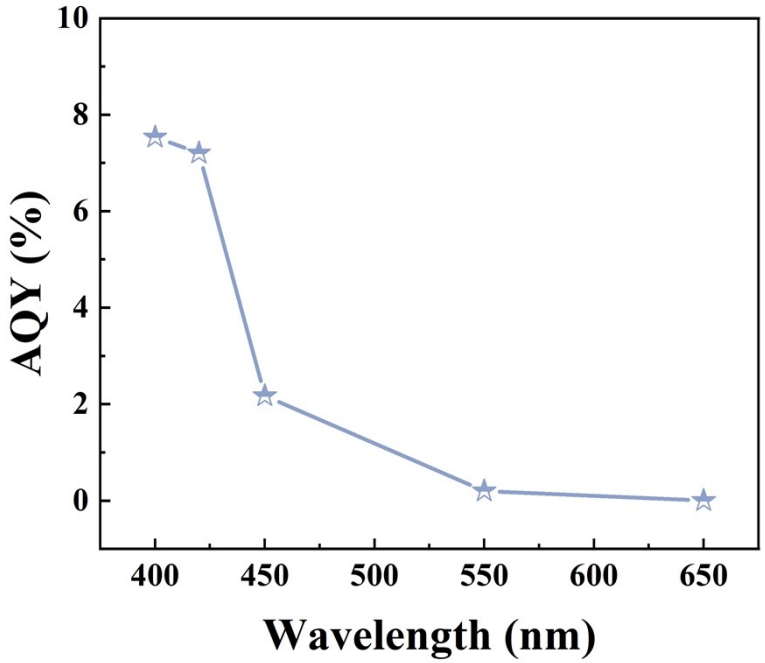

Fig. S16. The wavelength-dependent AQY of **$[Cu_{14}][O@Cu_{14}]@g\text{-}C_3N_4(OH)$** for photocatalytic H_2 evolution.

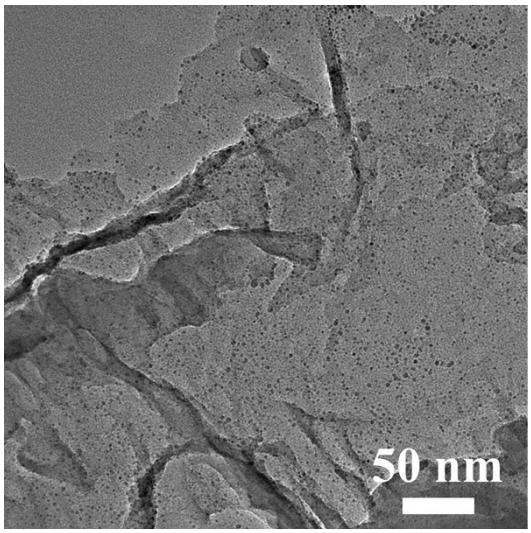

Fig. S17. The TEM image of **$[Cu_{14}][O@Cu_{14}]@g\text{-}C_3N_4(OH)$** after photocatalytic H_2 evolution.

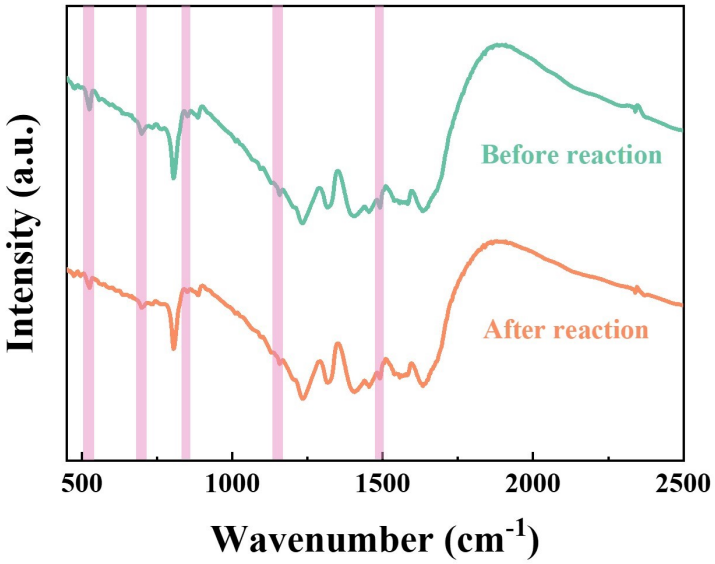

Fig. S18. The FTIR spectrum of **$[Cu_{14}][O@Cu_{14}]@g\text{-}C_3N_4(OH)$** after photocatalytic H_2 evolution.

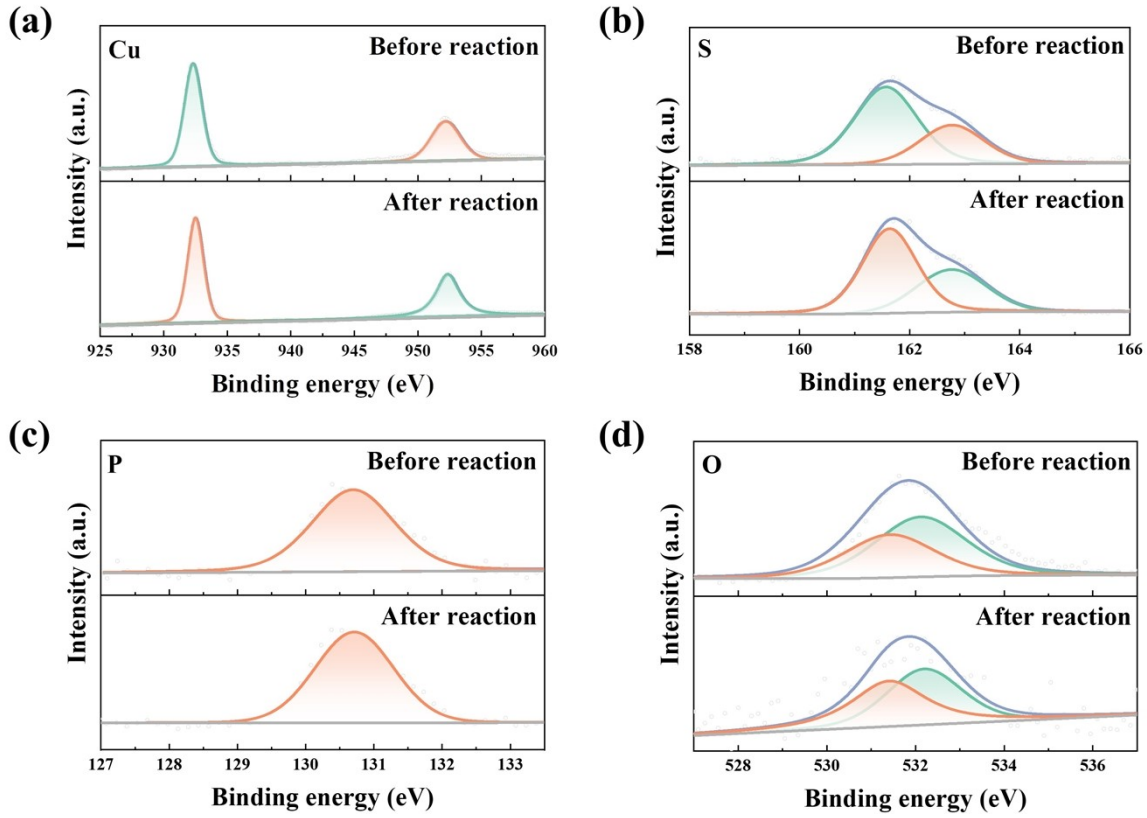

Fig. S19. XPS spectra for Cu 2p (a), S 2p (b), P 2p (c) and O 1s (d) of **$[Cu_{14}][O@Cu_{14}]$@g-C_3N_4(OH)** after photocatalytic H_2 evolution.

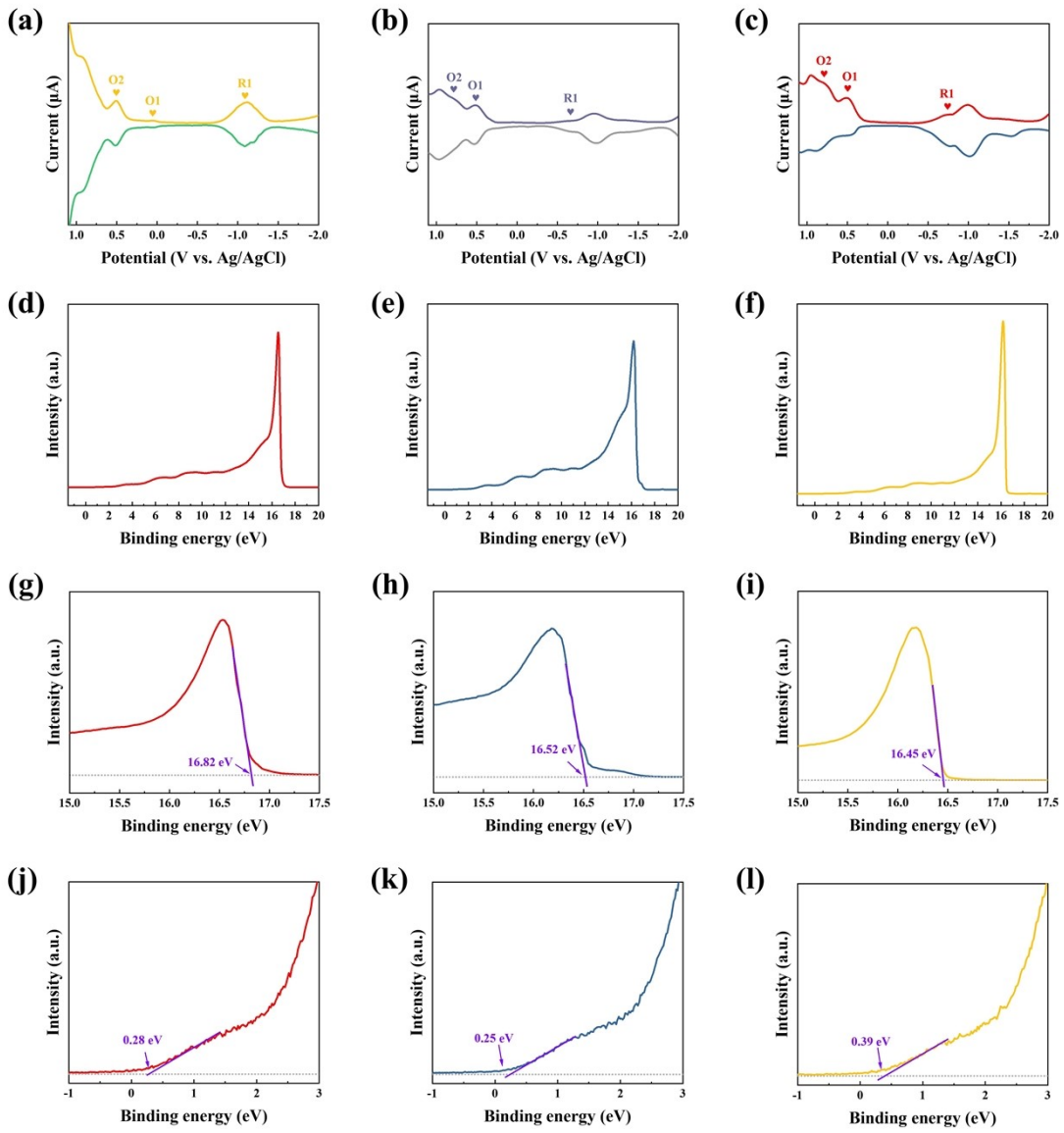

Fig. S20. DPV of $\mathbf{Cu_{14}}$ (a), $\mathbf{O@Cu_{14}}$ (b) and $\mathbf{[Cu_{14}][O@Cu_{14}]}$ (c). The UPS spectra of $\mathbf{Cu_{14}}$ (d), $\mathbf{O@Cu_{14}}$ (e) and $\mathbf{[Cu_{14}][O@Cu_{14}]}$ (f). The energies of the secondary electron cutoff edge of $\mathbf{Cu_{14}}$ (g), $\mathbf{O@Cu_{14}}$ (h) and $\mathbf{[Cu_{14}][O@Cu_{14}]}$ (i). The energies of the injection potential barrier edge of $\mathbf{Cu_{14}}$ (j), $\mathbf{O@Cu_{14}}$ (k) and $\mathbf{[Cu_{14}][O@Cu_{14}]}$ (l).

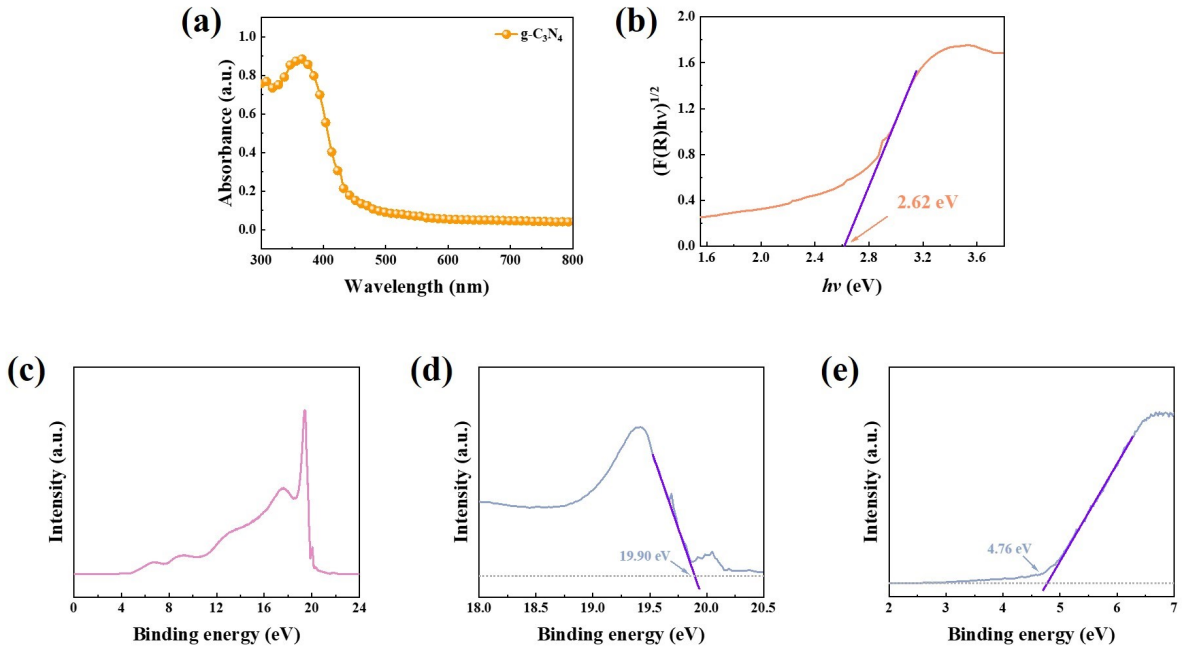

Fig. S21. (a) The UV-Vis diffuse reflectance spectrum of g-C_3N_4(OH). (b) The bond gap of g-C_3N_4(OH) estimated by the Tauc plot of KubelkaMunk function: $((\alpha hv)^2 = C(hv - E_g))$. (c) The UPS spectra g-$C_3N_4$(OH). (d) The energies of the secondary electron cutoff edge of g-C_3N_4(OH). (e) and the energies of the injection potential barrier edge of g-C_3N_4(OH).

Table S1. Metric Data of the Known Clusters of with Cu_8 cages encapsulating central atoms.

Compound	Central atom	Average Cu-Cu distance (Å)	*Ref.*
$[AuCu_{14}(TBBT)_{12}(TPP)_6]^+$	Au	3.110	*5*
$[AuCu_{14}(TBBT)_{12}(TTP)_6]^+$	Au	3.091	*5*
$[AuCu_{14}(TBBT)_{12}(T^{P}TPP)_6]^+$	Au	3.078	*5*
$Au@Cu_{14}$	Au	3.132	*6*
$[AuCu_{14}(SR)_{12}(PPh_3)_6]^+$	Au	3.123	*7*
$[Cu_8(\mu_8\text{-}Br)\{Se_2P(OR)_2\}_6]$	Br	3.171	*8*
$Cu_8(\mu_8\text{-}Br)[Se_2P(OPr^i)_2]_6$	Br	3.180	*9*
$[Cu_8(\mu_8\text{-}Se)[Se_2P(OPr^i)_2]_6]$	Se	2.928	*10*
$Cu_8(\mu_8\text{-}Se)[Se_2P(OR)_2]_6$	Se	2.905	*11*
$Cl@Cu_{14}$	Cl	3.253	*6*
$[Cu_{14}(D\text{-}Pen)_{12}Cl]^{5-}$	Cl	3.302	*12*
$[Cu_{14}(SC(CH_3)_2COO)_{12}Cl]^{5-}$	C1	3.355	*13*
$\{Cu_8[S_2P(OR)_2]_6(\mu_8\text{-}S)\}$	S	3.010	*14*
$Cu_8(\mu\text{-}I)(\mu_6\text{-}S)(DTP)_6$	S	3.163	*15*
$\{Cu_8[S_2P(O^iPr)_2]_6(\mu_8\text{-}S)\}$	S	3.111	*16*
$[Cu_8(F)(S_2P(O^iPr)_2)_6]^+$	F	3.035	*17*
$[Cu_8(F)(S_2P(OEt)_2)_6]^+$	F	2.971	*17*
1	-	2.685	*This work*
2	O	2.710	*This work*
3	O	2.786	*This work*

Table S2. Comparison of photocatalytic H_2 evolution activities of crystalline Cu-based photocatalysts.

Catalyst	Sacrificial agent	Solvent	H_2 evolution	AQY/TON	*Ref.*
Cu_{14}@g-C_3N_4(OH)	TEOA	H_2O	0.96 mmol g^{-1} h^{-1}	-	*This work*
O@Cu_{14}@g-C_3N_4(OH)	TEOA	H_2O	1.17 mmol g^{-1} h^{-1}	-	*This work*
[Cu_{14}][O@Cu_{14}]@g-C_3N_4(OH)	TEOA	H_2O	1.53 mmol g^{-1} h^{-1}	AQY = 7.2% at 420 nm	*This work*
Cu-X-bpy	MeOH	TEA	7.09 mmol g^{-1} h^{-1}	-	18
Cu-RSH	TEOA	EtOH/H_2O	7.88 mmol g^{-1} h^{-1}	AQY = 4% (≥ 420 nm)	19
Cu-TiO_2 NFs/g-C_3N_4	TEOA	H_2O	1303 μmol g^{-1} in 5 h	-	20
{[$Cu^ICu^{II}_2$-(DCTP)$_2$]NO_3·1.5DMF}$_n$	MeOH	H_2O	160 μmol g^{-1} in 5 h	AQY = 2.3% at 420 nm	21
[Cu_4(DNP)(SCN)Cl_4]$_n$/H_2PtCl_6	CH_3OH	H_2O	27.5μmol g^{-1} h^{-1}	-	22
Cu^{2+}/Cu_2O/Cu	TEA	H_2O	0.71 mL/h	TOF = 173 h^{-1}	23
Cu-salen	TEA	H_2O	-	TON = 85 in 3 h	24
Cu(pyDAT)$_2$(NO_3)$_2$	TEOA	DMF	0.48 mmol/h	TOF = 314 min^{-1}	25

References

(1) CrysAlisPro 2012, Agilent Technologies. Version 1.171.36.31.

(2) G. M. Sheldrick, *Acta Cryst. A*, 2015, **71**, 3-8.

(3) O. V. Dolomanov, L. J. Bourhis, R. J. Gildea, J. A. K. Howard, H. Puschmann, *J. Appl. Cryst.*, 2009, **42**, 339-341.

(4) K. Brandenburg, *Diamond*, 2010.

(5) H. Li, F. Song, D. Zhu, Y. Song, C. Zhou, F. Ke, L. Lu, X. Kang, M. Zhu, *J. Am. Chem. Soc.*, 2022, **144**, 4845-4852.

(6) Y. Song, Y. Li, M. Zhou, X. Liu, H. Li, H. Wang, Y. Shen, M. Zhu, R. Jin, *Sci. Adv.*, 2021, **7**, eabd2091.

(7) H. Shen, Y.-Z. Han, Q. Wu, J. Peng, B. K. Teo, N. Zheng, *Small methods*, 2021, **5**, 2000603.

(8) C. W. Liu, C.-M. Hung, B. K. Santra, Y.-H. Chu, J.-C. Wang, Z. Lin, *Inorg. Chem.*, 2004, **43**, 4306-4314.

(9) C. W. Liu, C.-M. Hung, H.-C. Chen, J.-C. Wang, T.-C. Keng, K. Guo, *Chem. Commun.*, 2000, 1897-1898.

(10) C. W. Liu, H.-C. Chen, J.-C. Wang, T.-C. Keng, *Chem. Commun.*, 1998, 1831-1832.

(11) C.-W. Liu, C.-M. Hung, J.-C. Wang, T.-C. Keng, *J. Chem. Soc., Dalton Trans.*, 2002, 3482-3488.

(12) O. J. M. W. L. Birker, H. C. Freeman, *J. Am. Chem. Soc.*, 1977, **99**, 6890-6899.

(13) P. J. M. W. L. Birker, *Inorg. Chem.*, 1979, **18**, 3502-3506.

(14) D. Rusanova, K. E. Christensen, I. Persson, K. J. Pike, O. N. Antzutkin, X. Zou, R. Dupree, W. Forsling, *J. Coord. Chem.*, 2007, **60**, 517-525.

(15) Y. B. Chen, Z.-J. Li, Y.-Y. Qin, Y. Kang, J.-K. Cheng, R.-F. Hu, Y.-H. Wen, Y.-G. Yao, *Inorg. Chem. Commun.*, 2003, **6**, 405-407.

(16) C. W. Liu, T. Stubbs, R. J. Staples, J. P. Jr. Fackler, *J.Am.Chem.Soc.*, 1995, **117**, 9778-9779.

(17) C. Latouche, S. Kahlal, E. Furet, P.-K. Liao, Y.-R. Lin, C.-S. Fang, J. Cuny, C. W. Liu, J.-Y. Saillard, *Inorg. Chem.*, 2013, **52**, 7752-7765.

(18) D. Y. Shi, R. Zheng, M.-J. Sun, X. R. Cao, C.-X. Sun, C.-J. Cui, C.-S. Liu, J. W. Zhao, M. Du, *Angew. Chem. Int. Ed.*, 2017, **56**, 14637-14641.

(19) X.-Y. Dong, M. Zhang, R.-B. Pei, Q. Wang, D.-H. Wei, S.-Q. Zang, Y.-T. Fan, T. C. W. Mak, *Angew. Chem. Int. Ed.*, 2016, **55**, 2073-2077.

(20) H. Khan, H. Charles, C. S. Lee, *Appl. Surf. Sci*., 2023, **607**, 155068.

(21) Z.-L. Wu, C.-H. Wang, B. Zhao, J. Dong, F. Lu, W.-H. Wang, W.-C. Wang, G.-J. Wu, J.-Z. Cui, P. Cheng, *Angew. Chem. Int. Ed.*, 2016, **55**, 4938 -4942.

(22) L. Li, L. Huang, Z.-Y. Liu, X.-J. Zhao, E.-C. Yang, *Z. Anorg. Allg. Chem.*, 2019, **645**, 623-630.

(23) S. Cao, C.-J. Wang, G.-Q. Wang, Y. Chen, X.-J. Lv, W.-F. Fu, *RSC Adv.*, 2020, **10**, 5930-5937.

(24) C.-B. Li, Y. L. Chu, J. J. He, J. J. Xie, J. W. Liu, N. Wang, J. W. Tang, *ChemCatChem*, 2019, **11**, 1-9.

(25) S. Rajak, O. Schott, P. Kaur, T. Maris, G. S. Hanan, A. Duong, *Polyhedron*, 2020, **180**, 114412.